




An Omni-Azimuth Angle Sensor for Tilt Measuring Based on FBG Array

Guangwei Fu , Jiaqi Cao, Jiatong Zhang, Xinghu Fu , Wa Jin, and Weihong Bi 

Abstract—An omni-azimuth angle sensor for tilt measuring based on fiber Bragg grating (FBG) array is proposed. It is designed based on the sensitivity of FBG to axial traction. The sensor consists of a mass block and a cube frame connected by an FBG array. The FBG array consists of four FBGs. When the sensor is tilted at different angles, the axial traction of each FBG will change due to the pull of the mass block. The tilt angle of the sensing unit can be obtained by calculating the magnitude and direction of the resultant traction of the four FBGs. The array design and measurement theory of the sensor are introduced, and the sensitivity of the sensor is discussed. Experimental results show that the FBG array can be used to measure the omni-azimuth angle. The angle sensitivity varies unevenly with the tilt angle and the range of variation is $0.08 \text{ nm}/^\circ$ to $0.4593 \text{ nm}/^\circ$. Using the spectrometer with an accuracy of 0.01 nm , the angle resolution ranges from 0.125° to 0.0218° . The array effectively extends the measurement range of the tilt sensor, and reduces the number of FBGs as much as possible on the basis of achieving omni-azimuth angle measurement.

Index Terms—Fiber bragg grating (FBG), angle sensor, omni-azimuth, axial traction.

I. INTRODUCTION

WITH the rapid development of modernization, a large number of engineering structures emerge at the historic moment. Angle sensor plays an important role in engineering structure state detection. It is widely used in civil engineering [1], mechanical manufacturing [2], geophysical observation [3] and aeronautical engineering [4]. The existing angle sensors are mainly divided into electric [5]–[7], magnetic [8]–[11] and optical fiber [12]–[15]. Optical fiber angle sensor [16]–[19] not only has the unique advantages of optical fiber sensor [20]–[22], such as against electromagnetic interference, but also has the measurement accuracy and sensitivity no lower than the first two [23]–[24]. For example, Xiaotong Zhang *et al.* [25] proposed an angle sensor based on the multi-mode photonic crystal fiber interference principle. A multi-mode photonic crystal fiber was

fused between two single-mode fibers and placed in a glass tube containing NaCl solution. The angle was measured by monitoring the change of liquid level, and the measurement sensitivity is $-1.5461 \text{ nm}/^\circ \sim -30.1244 \text{ nm}/^\circ$. Junjie Wang *et al.* [26] proposed using three independent ultra-fine fiber probes to construct a highly sensitive two-dimensional fiber inclinometer. By monitoring the displacement of the three reflected wavelengths, the angle and direction of tilt can be deduced simultaneously. The inclinometer has a tilt angle measurement resolution of less than 0.0004° and a measurement range of $\pm 5^\circ$.

With the rapid development of science and military technology, the measurement technology of tilt angle in a single plane is more and more difficult to meet the needs of the society, and the tilt angle in any direction needs to be measured. Therefore, angle sensors are developing in the three-dimensional direction [27]–[30]. For example, Jingxian Cui *et al.* [31] wrote FBG on the center core and two outer cores of the seven-core optical fiber, and observed the wavelength drift of each FBG during tilt to measure the angle. The detection range of azimuth angle is $0^\circ \sim 360^\circ$, and the minimum measurement error is 0.0056° . The detection range of tilt angle is $0^\circ \sim 90^\circ$, and the minimum error of measurement is 0.025° .

In this paper, the sensitivity of fiber grating to axial traction is used to measure the tilt angle. Because the response sensitivity of FBG to axial traction is higher than that of LPFG, an FBG array is designed in this paper. The mass block is connected to the cube frame through the FBG array, and the omni-azimuth angle is measured by judging the traction of each FBG. At present, the existing FBG sensors that use the internal inertial elements of the sensors for angle measurement usually need six FBGs [32], but this paper realizes the omni-azimuth angle measurement by using four FBGs, it reduces the number of FBGs as much as possible, which is also the most valuable part of this research.

II. SENSOR STRUCTURE AND MEASUREMENT PRINCIPLE

A. Structural Design of the Sensor

In the angle sensor designed in this paper [32], the mass block and the cube frame are connected by four FBGs (L1 grating, L2 grating, L3 grating and L4 grating) with different resonant wavelengths. The coordinate system as shown in Fig. 1 is established. The origin of the coordinate system is at the center of the cube frame, and when the sensing unit is tilted, the coordinate system is fixed, it is not tilt with the sensor. L1 and L2 gratings are located in the xOz plane, while L3 and L4 gratings are located in the yOz plane. Point O is the location of

Manuscript received August 22, 2021; revised September 29, 2021; accepted October 7, 2021. Date of publication October 14, 2021; date of current version November 10, 2021. This work was supported in part by the S&T Program of Hebei Province under Grant 216Z1706G, in part by the National Natural Science Foundation of China under Grant 61675176, in part by the S&T Program of Hebei Province under Grants F2021203045, 216Z1702G, and F2021203058, and in part by the S&T Program of Hebei Province under Grant 17961701D. (Corresponding author: Guangwei Fu.)

The authors are with the School of Information Science and Engineering, The Key Laboratory for Special Fiber and Fiber Sensor of Hebei Province, Yanshan University, Qinhuangdao 066004, China (e-mail: earl@ysu.edu.cn; 985384758@qq.com; 757200373@qq.com; fuxinghu@ysu.edu.cn; jinwa@ysu.edu.cn; whbi@ysu.edu.cn).

Digital Object Identifier 10.1109/JPHOT.2021.3119896

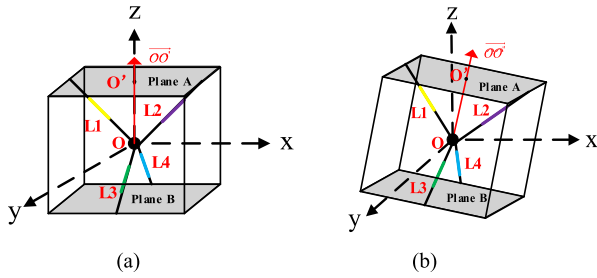


Fig. 1. Schematic diagram of tilt angle sensor: (a) Vertical state and coordinate system and (b) Tilt state.

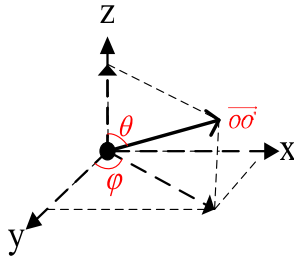


Fig. 2. Geometric diagram of the angles of tilt.

the mass block, which is the center of the cube frame; Point O' is the center of the top surface of the cube; The vector $\overrightarrow{OO'}$ is defined as the normal vector of the sensing unit.

The equations for the location of the four FBGs are

$$\begin{cases} L1 : x = -z (x < 0) \\ L2 : x = z (x > 0) \\ L3 : y = -z (y > 0) \\ L4 : y = z (y < 0) \end{cases} \quad (1)$$

According to the Eq. (1), L1 and L2 are located in the xOz plane, and they are at a 45° angle to the positive half of the Z -axis; L3 and L4 are located in the yOz plane, and they are at a 45° angle to the negative half of the Z -axis.

In order to express the angle conveniently, we define the tilt angle and the tilt direction. The schematic diagram is shown in Fig. 2. θ is the tilt angle (The angle between the normal vector $\overrightarrow{OO'}$ and the positive half of the Z -axis, in the range of $[0^\circ, 360^\circ]$), φ is the tilt direction (The angle between the positive half of the X -axis and the projection of $\overrightarrow{OO'}$ onto the xOy plane, in the range of $[0^\circ, 180^\circ]$).

When the FBGs are fixed, an initial traction is given to each FBG so that the mass block is located at the center of the cube frame. When the sensing unit is tilted, the traction on each FBG changes. By analyzing the traction of each FBG, the tilt direction and tilt angle of the sensing unit can be determined. Compared with the cube frame, the mass block has a smaller volume, so it can be regarded as a particle, and the stretch length of FBG under traction is negligible relative to the volume of the sensing unit. Therefore, in the process of angle measurement, it can be regarded as that the mass block has been fixed at the center of the cube frame without displacement. In other words, the angle between each FBG line and the cube frame remains unchanged.

The traction analysis shows that the traction of mass block in the positive direction of X -axis can be calculated by the projection of the traction of L2 grating on the positive half of X -axis. The traction of mass block in the negative direction of the X -axis can be calculated by the projection of the L1 grating traction in the negative half of the X -axis. The traction of mass block in the positive direction of Y -axis can be calculated by the projection of L3 grating on the positive half of Y -axis. The traction of mass block in the negative direction of the Y -axis can be calculated by the projection of L4 grating on the negative half of the Y -axis. The traction of mass block in the positive direction of the Z -axis can be calculated by the component traction of L1 grating and L2 grating in the positive half of the Z -axis. The traction of mass block in the negative direction of the Z -axis can be calculated by the component traction of L3 grating and L4 grating in the negative half of the Z -axis. Therefore, the array can measure omni-azimuth angle.

B. Measurement Principle of the Sensor

According to the coupled mode theory of FBG, the light transmission mechanism of FBG is forming narrow-band reflection by coupling the forward and backward transmission guide modes. Its grating equation is [33]:

$$\lambda = 2n_{\text{eff}}\Lambda \quad (2)$$

Where, n_{eff} is the effective refractive index of the transmission guide mode; λ is the resonant wavelength of FBG; Λ is the period of FBG.

According to the Eq. (2), the λ depends on the Λ and the n_{eff} . When FBG is subjected to axial traction, its period and effective refractive index are changed, and the resonant wavelength is shifted. By extracting the resonant wavelength drift of FBG before and after under the traction, the traction on FBG can be obtained.

It is assumed that FBG is acted on only by axial traction, and other parameters remain constant. Under the action of axial traction, FBG will shrink or stretch to different degrees. In this case, the traction on FBG in all directions can be expressed as $\sigma_z = -P$ (P is the applied traction), $\sigma_x = \sigma_y = 0$. According to Hooke's theorem $\varepsilon_z = -P/E$, the strain in each direction is

$$\begin{aligned} \varepsilon_j &= [\varepsilon_x \ \varepsilon_y \ \varepsilon_z \ 0 \ 0 \ 0]^T \\ &= [-\nu\varepsilon_z \ -\nu\varepsilon_z \ \varepsilon_z \ 0 \ 0 \ 0]^T \\ &= [v\frac{P}{E} \ v\frac{P}{E} \ -\frac{P}{E} \ 0 \ 0 \ 0]^T \end{aligned} \quad (3)$$

Where, E is the elastic modulus of the quartz fiber in which FBG is located; ν is Poisson's ratio of optical fiber; ε is the change in length. According to Eq. (3), the wavelength drift of FBG under this traction can be expressed as:

$$\Delta\lambda_B = 2\Lambda \left(\frac{\partial n_{\text{eff}}}{\partial L} \Delta L + \frac{\partial n_{\text{eff}}}{\partial a} \Delta a \right) + 2\frac{\partial \Lambda}{\partial L} \Delta L n_{\text{eff}} \quad (4)$$

Where, $\frac{\partial n_{\text{eff}}}{\partial L}$ is the amount of refractive index change due to elasto-optic effect; $\frac{\partial n_{\text{eff}}}{\partial a}$ is the amount of refractive index change due to waveguide effect; ΔL is the expansion amount of optical

fiber along the Z direction; $\Delta\lambda$ is the variation of optical fiber diameter under axial traction. In general, the influence of the waveguide effect is negligible. The change amount of FBG gate pitch caused by axial traction is:

$$\Delta\lambda = \lambda \cdot \varepsilon_z \quad (5)$$

According to the theory of refractive index ellipsoid, For the refractive index change caused by the elasto-optical effect, the relation between the relative dielectric impermeability tensor and the dielectric constant is as follows:

$$\beta_{ij} = \frac{1}{\varepsilon_{ij}} = \frac{1}{n_{ij}^2} \quad (6)$$

Where, β_{ij} is the relative dielectric impermeability tensor; n_{ij} is the refractive index of optical fiber in a certain direction; ε_{ij} is the dielectric constant.

When the optical fiber is subjected to axial traction, β_{ij} changes, and the Eq. (6) can be deformed into:

$$\Delta(\beta_{ij}) = \Delta\left(\frac{1}{n_{ij}^2}\right) = -\frac{2\Delta n_{\text{eff}}}{n_{\text{eff}}^3} \quad (7)$$

the effective index change is denoted as:

$$\Delta(\beta_{ij}) = \Delta\left(\frac{1}{n_{ij}^2}\right) = \sum_{j=1}^6 P_{ij}\varepsilon_j \quad (8)$$

Where $i = 1,2,3$ represent X, Y, and Z directions respectively. According to Eq. (3), Eq. (8) and the elasto-optical coefficient matrix of quartz fiber P_{ij} , we can get:

$$P_e = \frac{n_{\text{eff}}^2}{2} [P_{12} - \nu(P_{11} + P_{12})] \quad (9)$$

According to the above derivation, the resonant wavelength drift of FBG under axial traction conforms to the following model:

$$\begin{aligned} \frac{\Delta\lambda_{Bz}}{\lambda_B} &= \frac{1}{E} \left\{ -\frac{n_{\text{eff}}^2}{2} [(P_{11} + P_{12}) \cdot (-\nu) + P_{12}] + 1 \right\} \cdot \sigma_z \\ &= \frac{1}{E} (1 - P_e) \cdot \sigma_z \end{aligned} \quad (10)$$

When the sensing unit is tilted, each FBG will be subjected to different axial traction, and its resonant wavelength will drift. As the axial traction increases, the resonant wavelength has a red shift, and as the axial traction decreases, the resonant wavelength has a blue shift.

III. EXPERIMENTS AND ANALYSIS OF RESULT

A. Experiment Test System

The sensor unit designed is fabricated. FBGs with different resonant wavelengths were selected: L1 grating, L2 grating, L3 grating and L4 grating. The array is composed of four FBGs inscribed on independent fibers in a specific arrangement, unlike the array formed by multiple FBG inscribed on one fiber [34], [35]. The resonant wavelengths are: 1575 nm, 1545 nm, 1560 nm and 1590 nm respectively. In order to prevent the FBG from breaking during the measurement process, a spring is set outside the FBG. When be pulled, the spring converts the traction into

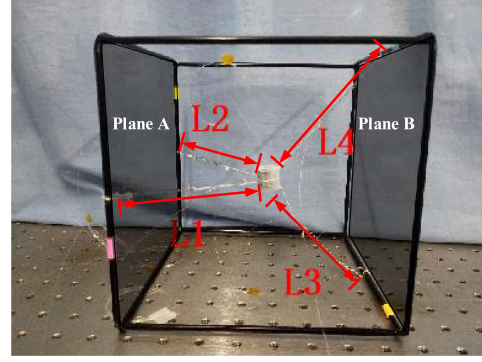


Fig. 3. Physical object of the angle sensing unit.

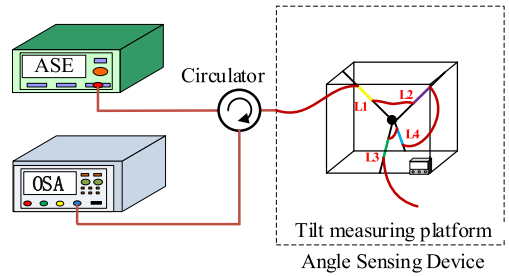


Fig. 4. Experiment setup for tilt angle measurement.

a small deformation on the FBG. The FBGs and the springs are fixed with glue at both ends. The length of the spring is 50 mm and the elastic coefficient is -131.25 g/mm. According to the designed array, both ends of the spring are connected with the cube frame and the mass block respectively by an inelastic rope. Tie the inelastic rope to the selected position of the cube frame and secure it with glue. The shape of mass block will affect the angle measurement result. In order to ensure that the angle measurement results in different directions are not affected by the shape of the mass block, a mass block with uniform shape in all directions needs to be selected. We chose the spherical mass for the experiment. The weight of the mass block is 30 g, and the length of sides of the cube frame is 20 cm. Finally, four FBGs with springs are cascaded. The required sensing unit is prepared. The picture of the angle sensing unit is shown in Fig. 3.

After the required sensing unit is prepared, the experimental system is set up for experiments. It is shown in Fig. 4.

The one end of the FBG sensing unit is hang in the air, and another end of the FBG sensing unit is connected with jumpers, which is connected with the optical spectrum analyzer (Optical Spectrum Analyzer AQ6375, OSA) and ASE broadband light source through circulator. The wavelength range of the light source is $1520 \sim 1610$ nm, and the maximum output optical power is 50 mW. The light output from the ASE enters the sensing unit through the circulator. After passing through the FBG array, most of the light is reflected back and then passed through the circulator and enters the OSA. During the experiment, we set up an electronic tiltmeter fixed on the sensing unit to calibrate the tilt angle. The tiltmeter is essentially a kind of acceleration sensor using the principle of inertia. When the tilt sensor is stationary, there is no acceleration in the lateral and

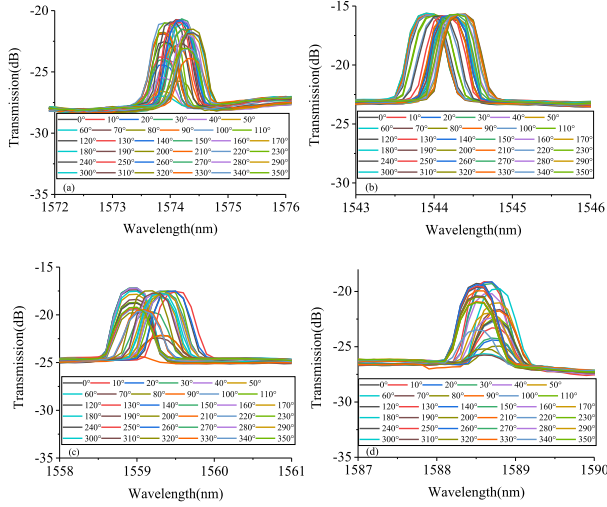


Fig. 5. When $\varphi = 0^\circ$, the experimental results of FBGs at different angles (a) L1, (b) L2, (c) L3, and (d) L4.

vertical directions, so only the acceleration of gravity is acting on it. The angle between the vertical axis of gravity and the sensitive axis of the acceleration sensor is the tilt angle. The tiltmeter can directly output angle value, and it can realize three-dimensional angle measurement ranges from 0° to 90° .

B. Sensor Tilt Calibration Tests

The mathematical model is established. The shift of resonant wavelength of each FBG is simulated and analyzed during the change of tilt angle. Model building is mainly divided into the following steps.

Step1: During the tilting process, there are at most three FBGs subjected to traction. Analyze which FBGs are subjected to traction at different tilt angles (θ, φ).

Consider the vectors from the coordinate origin to the grating as direction vectors for each grating. When the angle between the tilted normal vector and the grating vector is greater than 90° , the grating is not under traction. Conversely, when the angle is less than or equal to 90° , the grating is under traction.

Step2: Analyze the relationship between the traction received by each FBG and the tilt angles (θ, φ).

Step3: Use Matlab to calculate the traction on each FBG at different tilt angles (θ, φ).

Step4: Use coupled mode theory to calculate the resonant wavelengths of output spectrum at different tilt angles (θ, φ).

We conducted experiments based on the above models and compared the experimental results with the theoretical analysis results. Now we take the cases of $\varphi = 0^\circ$ and $\varphi = 45^\circ$ as examples.

The output spectrum obtained through experiments at different angles are as follows. The wavelengths at resonance peaks of each spectral line are extracted, and then compared with the theoretical analysis results. In the case of $\varphi = 0^\circ$, the resonance wavelengths changing with angle are as shown in Fig. 5. Comparison of experimental results and theoretical analysis results is shown in Fig. 6.

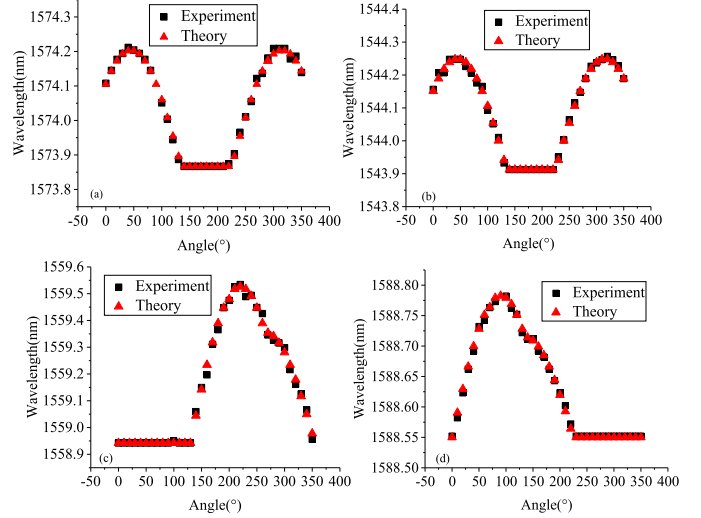


Fig. 6. When $\varphi = 0^\circ$, the comparison of simulation and experimental results of FBGs at different angles (a) L1, (b) L2, (c) L3, and (d) L4.

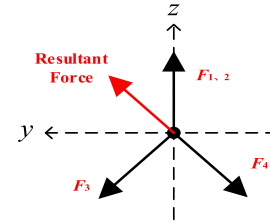


Fig. 7. Traction analysis diagram under the condition $\varphi = 0^\circ$.

The resonant wavelength of FBG without traction is called the minimum value, and the resonant wavelength when FBG pulls the mass block alone is called the maximum value. It is known that the resultant traction of the four FBGs is the same as the gravity of the mass block, but in the opposite direction. The traction analysis is shown in Fig. 7. When the sensing unit tilts 0° to 360° in the direction $\varphi = 0^\circ$, the vector of gravity starts at $\theta = 180^\circ$ in the yOz plane and rotates clockwise. The vector equivalent to the resultant traction of the four FBGs traction rotates clockwise starting at $\theta = 0^\circ$. Since L1 grating and L2 grating are symmetric about yOz plane, they have the same change rule during tilting.

According to theoretical analysis and contrast with the experiments, when $\theta = 0^\circ$, only L1 grating and L2 grating are under traction; When $0^\circ < \theta < 135^\circ$, only L1 gratings, L2 gratings and L4 gratings are under traction; When $\theta = 135^\circ$, only L4 grating is under traction; When $135^\circ < \theta < 225^\circ$, only L3 grating and L4 grating are under traction; When $\theta = 225^\circ$, only L3 grating is under traction; When $225^\circ < \theta < 360^\circ$, only L1 gratings, L2 gratings and L3 gratings are under traction. When the sensing unit rotates 360° along the direction $\varphi = 0^\circ$, the change of resonance wavelengths of L1 grating, L2 grating, L3 grating and L4 grating are analyzed as follows.

For L1 and L2, when $0^\circ \leq \theta \leq 45^\circ$, the axial traction on the L1 grating and L2 grating gradually increase. Their resonant wavelengths have a red shift and reach the maximum value at

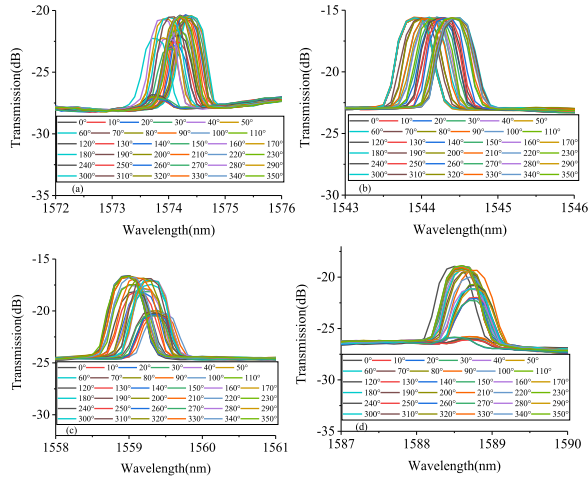


Fig. 8. When $\varphi = 45^\circ$, the experimental results of FBGs at different angles (a) L1, (b) L2, (c) L3, and (d) L4.

45° . When $45^\circ \leq \theta \leq 135^\circ$, the axial traction on L1 grating and L2 grating decrease, their resonant wavelengths have a blue shift and reach the minimum value at 135° . When $135^\circ \leq \theta \leq 225^\circ$, L1 grating and L2 grating are not under traction, and their resonant wavelength remain the minimum value constant; When $225^\circ \leq \theta \leq 315^\circ$, the axial traction of L1 grating and L2 grating increase, and their resonant wavelengths have a red shift; When $315^\circ \leq \theta \leq 360^\circ$, the axial traction of L1 grating and L2 grating decrease and their resonant wavelengths have a blue shift.

For L3, when $0^\circ \leq \theta \leq 135^\circ$, L3 grating is not under traction and the resonant wavelength does not drift; When $135^\circ < \theta \leq 225^\circ$, the axial traction on the L3 grating increases, and the resonant wavelength has a red shift, reaching its maximum value at 135° . When $225^\circ < \theta < 360^\circ$, the axial traction on the L3 grating decreases, and the resonant wavelength has a red shift.

For the L4, when $0^\circ \leq \theta \leq 135^\circ$, the axial traction on the L4 grating increases, and the resonant wavelength has a red shift, reaching its maximum value at 135° . When $135^\circ < \theta \leq 225^\circ$, the axial traction on the L4 grating decreases and the resonant wavelength has a blue shift. When $225^\circ < \theta < 360^\circ$, the L4 grating is not under traction, the resonant wavelength does not drift, and the minimum value remains unchanged.

In the case of $\varphi = 45^\circ$, the resonance wavelength changing with angle as shown in Fig. 8. Comparison of experimental results and theoretical analysis results is shown in Fig. 9.

According to theoretical analysis and contrast with the experiments, when $\theta = 0^\circ$, only L1 grating and L2 grating are under traction; When $0^\circ < \theta < 90^\circ$, only L1 gratings, L2 gratings and L4 gratings are under traction; When $\theta = 90^\circ$, only L1 grating and L4 grating are under traction; When $90^\circ < \theta < 180^\circ$, only L1 gratings, L3 gratings and L4 gratings are under traction; When $\theta = 180^\circ$, only L3 grating and L4 grating are under traction; When $180^\circ < \theta < 270^\circ$, only L2 grating, L3 grating and L4 grating are under traction; When $\theta = 270^\circ$, only L2 grating and L3 grating are under traction; When $270^\circ < \theta < 360^\circ$, only L1 gratings, L2 gratings and L3 gratings are under traction. When the sensing unit rotates 360° along the direction $\varphi = 45^\circ$, the

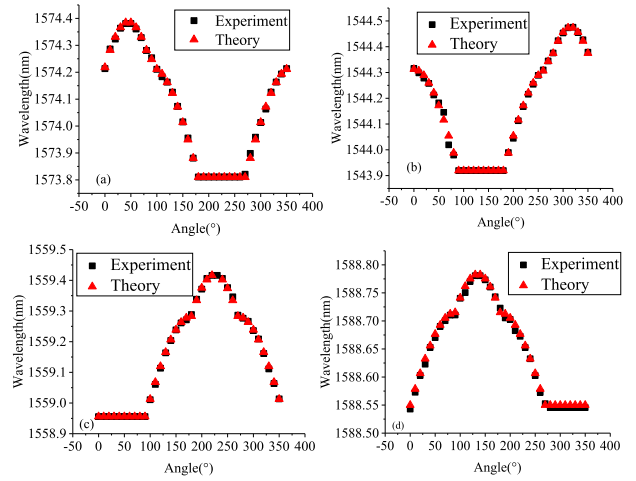


Fig. 9. When $\varphi = 45^\circ$, the comparison of simulation and experimental results of FBGs at different angles (a) L1, (b) L2, (c) L3, and (d) L4.

change of resonance wavelengths of L1 grating, L2 grating, L3 grating and L4 grating are analyzed as follows.

For L1, when $0^\circ \leq \theta \leq 45^\circ$, the traction of L1 grating increases gradually. The resonant wavelength has a red shift and reaches the maximum value at 45° . When $45^\circ \leq \theta \leq 180^\circ$, the traction of L1 grating decreases gradually, the resonant wavelength has a blue shift, and reaches the minimum value at 180° . When $180^\circ \leq \theta \leq 270^\circ$, L1 grating is not under traction, and the resonant wavelength remains the minimum constant; When $270^\circ \leq \theta \leq 360^\circ$, the traction of L1 grating increases, and the resonant wavelength has a red shift.

For L2, when $0^\circ \leq \theta \leq 90^\circ$, the axial traction on L2 grating gradually decreases, and the resonant wavelength has a blue shift, reaching the minimum value at 90° . When $90^\circ \leq \theta < 180^\circ$, the L2 grating is not under traction, and the resonant wavelength keeps the minimum constant. When $180^\circ \leq \theta \leq 270^\circ$, the traction of L2 grating increases gradually, and the resonant wavelength has a red shift, reaching the maximum value at 270° . When $270^\circ \leq \theta \leq 360^\circ$, the traction of L2 grating decreases gradually, and the resonant wavelength has a blue shift.

For L3, when $0^\circ \leq \theta \leq 90^\circ$, the L3 grating is not under traction, and the resonant wavelength keeps the minimum value unchanged. When $90^\circ < \theta \leq 225^\circ$, the axial traction on the L3 grating increases gradually, and the resonant wavelength has a red shift, reaching its maximum value at 225° . When $225^\circ \leq \theta < 360^\circ$, the axial traction on the L3 grating decreases gradually, and the resonant wavelength has a blue shift until it reaches the minimum value at 360° .

For L4, when $0^\circ \leq \theta < 135^\circ$, the axial traction on the L4 grating increases gradually, and the resonant wavelength has a red shift, reaching the maximum value at 135° . When $135^\circ \leq \theta \leq 270^\circ$, the axial traction on the L4 grating decreases gradually, the resonant wavelength has a blue shift and reaches the minimum value at 270° . When $270^\circ < \theta < 360^\circ$, the L4 grating is not under traction and the resonant wavelength remains the minimum constant.

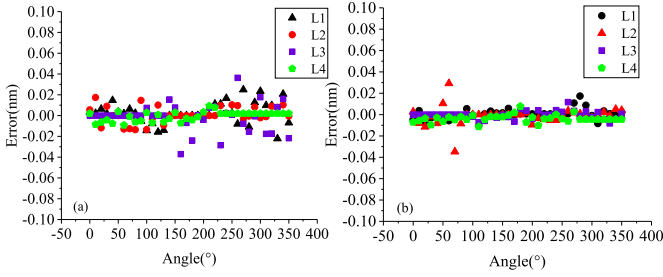


Fig. 10. Error analysis: (a) $\varphi = 0^\circ$ and (b) $\varphi = 45^\circ$.

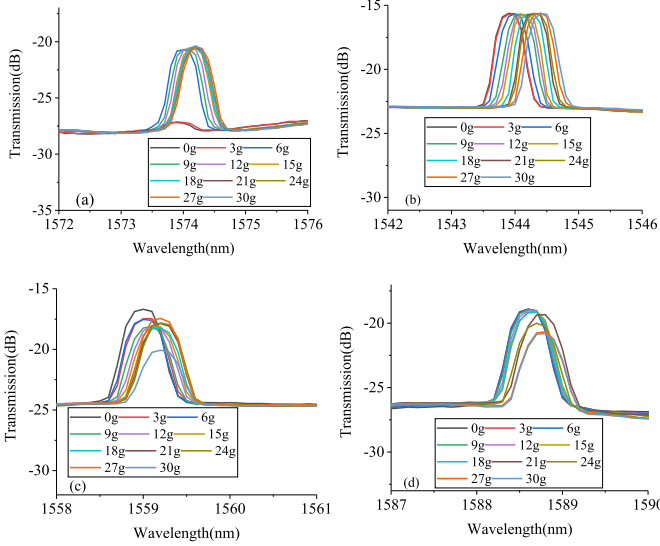


Fig. 11. The experimental results of FBG at different tilt angles: (a) L1, (b) L2, (c) L3, and (d) L4.

The difference between the theoretical analysis results and the experimental results is calculated and the error analysis is shown in Fig. 10. As can be seen from the figure, the error is kept within the range of $0 \sim 0.03$ nm, which does not affect the solution of angle.

C. Angle Calculation

The essence of the FBG's omni-azimuth angle measurement is achieved through traction measurement. The measurement sensitivity depends on the response sensitivity of each FBG to axial traction. Therefore, before analyzing the sensitivity, the relationship between the traction on FBG and the output spectrum should be analyzed. We measured the axial traction of the four FBG's respectively. Using each FBG to suspend the mass block vertically, the axial traction on the FBG is changed by changing the weight of the mass block, which varies from 0g to 30g with an interval of 3g. The experimental results are shown in Fig. 11. Comparison of experimental results and theoretical analysis results is shown in Fig. 12.

By analyzing the experimental results, it can be seen that with the increase of axial traction on FBGs, their resonant wavelength will have a red shift. In addition, the wavelength drift keeps uniform changing in the process of uniform increase of traction, and the relationship between the two is linear. The sensitivity of

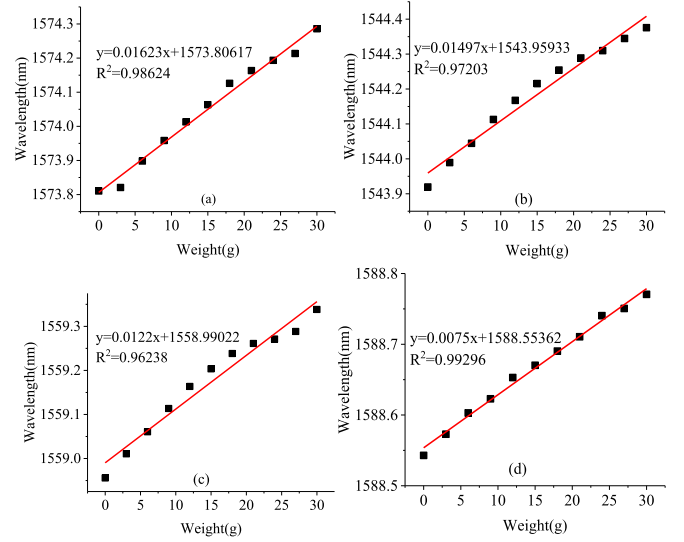


Fig. 12. Comparison of simulation and experimental results of FBG at different tilt angles: (a) L1, (b) L2, (c) L3, and (d) L4.

the four FBGs to traction response is 1.6174 nm/N, 1.5524 nm/N, 1.3012 nm/N and 0.7744 nm/N, respectively. The fitting equations will be used in multi-azimuth angle calculation and sensor sensitivity analysis. For this FBG array, the omni-azimuth tilt angle measurement through experiments is mainly carried out according to the following steps:

Step1: Extract the position information of each FBG resonant wavelength in the output spectrum.

Step2: Judge the traction of each FBG according to the extracted resonant wavelength.

Step3: On the basis of the coordinate system established in Fig. 1 and according to the traction decomposition, Eq. (11) is used to solve the vector components of the four FBGs resultant traction F on the X -axis, Y -axis and Z -axis, which is F_a, F_b, F_c , respectively.

$$\begin{cases} F_a = (F_2 - F_1) \cos 45^\circ \\ F_b = (F_3 - F_4) \cos 45^\circ \\ F_c = (F_1 + F_2 - F_3 - F_4) \cos 45^\circ \end{cases} \quad (11)$$

D. Sensitivity Analysis

The overall sensitivity of the FBG array sensor angle measurement is not only related to the traction response sensitivity of each FBG, but also related to the tilt angle. The sensitivity in the case of $\varphi = 0^\circ$ was taken as an example for analysis.

In the case of $\varphi = 0^\circ$, When $0^\circ < \theta < 135^\circ$, only L1 gratings, L2 gratings and L4 gratings are under traction; When $135^\circ < \theta < 225^\circ$, only L3 grating and L4 grating are under traction; When $225^\circ < \theta < 360^\circ$, only L1 gratings, L2 gratings and L3 gratings are under traction. When multiple gratings are under traction at the same time, the sensitivity of angle measurement depends on their average sensitivity. When $0^\circ < \theta < 135^\circ$, the

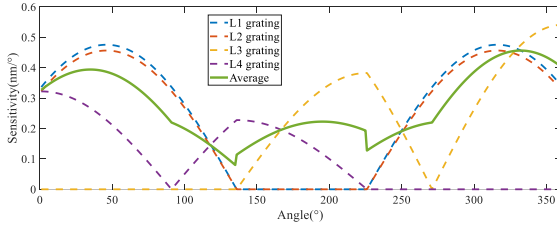


Fig. 13. When $\varphi=0^\circ$, The sensitivity at different tilt angles.

traction is

$$\begin{cases} F_1 = \frac{G \sin \theta - G \cos \theta}{2 \cos 45^\circ} \\ F_2 = \frac{G \sin \theta - G \cos \theta}{2 \cos 45^\circ} \\ F_3 = 0 \\ F_4 = \frac{G \sin \theta}{\cos 45^\circ} \end{cases} \quad (12)$$

When $135^\circ < \theta < 225^\circ$, the traction is

$$\begin{cases} F_1 = 0 \\ F_2 = 0 \\ F_3 = \frac{-G \cos \theta + G \sin \theta}{2 \cos 45^\circ} \\ F_4 = \frac{-G \cos \theta - G \sin \theta}{2 \cos 45^\circ} \end{cases} \quad (13)$$

When $225^\circ < \theta < 360^\circ$, the traction of L3 grating is

$$\begin{cases} F_1 = \frac{-G \sin \theta - G \cos \theta}{2 \cos 45^\circ} \\ F_2 = \frac{-G \sin \theta - G \cos \theta}{2 \cos 45^\circ} \\ F_3 = \frac{-G \sin \theta}{\cos 45^\circ} \\ F_4 = 0 \end{cases} \quad (14)$$

The derivative of Eq. (12), Eq. (13) and Eq. (14) is the change amount of the traction on the grating with the tilt angle changing by 1° , and then multiplied by their sensitivity to axial traction response respectively, which is the sensitivity of the sensing unit to the tilt angle measurement. The experimental results are shown in Fig. 13.

According to the Fig. 13, The sensitivity ranges from $0.08 \text{ nm}/^\circ$ to $0.4593 \text{ nm}/^\circ$. Using the spectrometer with an accuracy of 0.01 nm , the angle resolution ranges from 0.125° to 0.0218° . The variation is uneven throughout the tilting process. The same is true for sensitivity analysis in other tilt directions.

Compared to other angle sensors of the same type, this sensor can be used for omni-azimuth tilt angle measurement. Its angle measurement sensitivity is uneven with tilting different angles.

The advantage is that the least number of FBGs are used to achieve omni-azimuth tilt measurements, and the angle measurement sensitivity is not inferior.

E. Results Analysis

According to the above experimental results, it can be concluded that the angle sensor designed in this paper can realize omni-azimuth angle measurement, and the measurement sensitivity changes unevenly with tilting. Take case of $\varphi=0^\circ$ as an example, the sensitivity range is $0.08 \text{ nm}/^\circ$ to $0.4593 \text{ nm}/^\circ$. The comparison of this sensor with other existing sensors of the same type is shown in Table I. We can see that this sensor has the largest measurement range, and its measurement sensitivity is not inferior.

TABLE I
COMPARISON WITH OTHER TILT SENSORS

Reference	Configuration	Range	Sensitivity
Zhang et al, 2014[25]	Multi-mode photonic crystal fiber was fused between two single-mode fibers and placed in a glass tube containing NaCl solution.	$-35.1^\circ \sim 37.05^\circ$	$-1.55 \text{ nm}/^\circ \sim -30.12 \text{ nm}/^\circ$
Pan et al, 2017[16]	A pair of optical fiber collimators and a simple pendulum with an F-P filter were fit together	$-3^\circ \sim 3^\circ$	$1104 \text{ pm}/^\circ$
Cui et al, 2020[31]	FBG is encapsulated on the center core and two outer cores of the seven-core optical fiber	$0^\circ \sim 360^\circ$	$3.24 \text{ pm}/^\circ$
Guo et al, 2020[29]	FBG is encapsulated on both sides of the cam by double-end fixed packaging type	$-90^\circ \sim 90^\circ$	$29.68 \text{ pm}/^\circ \sim 46.71 \text{ pm}/^\circ$
This work	A mass block and a cube frame connected by FBG array	$0^\circ \sim 360^\circ$	$80 \text{ nm}/^\circ \sim 459.3 \text{ nm}/^\circ$

Since the wavelength drift of each FBG in the measurement process is taken as the parameter of the angle calculation, this array is somewhat deficient in solving the problem of temperature cross sensitivity. It can be considered to fix an addition LPFG on the cube frame for temperature compensation in the future practical application.

In addition, according to the light guiding principle of grating, the traction of FBG depends on its own deformation. Because the FBG and cube frame are connected by inelastic rope, which deforms almost nothing, the deformation of the FBG caused by the traction is mainly related to the size of the traction and the elastic coefficient of the spring. The length of the sides of the cube frame does not affect the experimental results. In this paper, in order to facilitate the experiment, the cube frame with larger length of sides and the longer FBGs are selected. In the future application, in order to reduce the volume of the sensor, the length of the cube side can be appropriately reduced and the FBGs with shorter length can be selected. Theoretically, the experimental results will not be affected.

The resolution of the sensor is related to the precision of the spectrometer. In this experiment, a spectrometer with precision of 0.01 nm was used and obtained the resolution from 0.125° C to 0.0218° C . Higher resolution can be measured when experiments are carried out with more accurate spectrometers.

IV. CONCLUSION

An Omni-azimuth angle sensor based on FBG array is designed and implemented. It consists of four FBGs connected with a mass block and a cube frame. The output spectra of the designed FBG array at different tilt angles are analyzed theoretically, and the experimental results are compared with the theoretical analysis results. The results show that the array can measure the tilt angle at omni-azimuth. Compared with existing fiber optic angle sensors of the same type, the number of FBGs used is reduced as far as possible. It also has great advantages in measuring range. The sensitivity of the sensor's angle measurement depends on the sensitivity of each FBG

to the traction response. Because the sensitivity of each FBG is different, it should be analyzed separately according to the situation. Take case of $\varphi=0^\circ$ as an example, the sensitivity range is $0.08 \text{ nm}/^\circ$ to $0.4593 \text{ nm}/^\circ$. Using the spectrometer with an accuracy of 0.01 nm , the angle resolution ranges from 0.125° to 0.0218° .

REFERENCES

- [1] R. Q. Lan, B. Feng, and Q. L. Shi, "Study on measuring dynamic deflection of high-speed railway bridge by angle meter," *World Earthq. Eng.*, vol. 36, no. 1, pp. 56–62, Apr. 2020.
- [2] J. C. Si and W. Cui, "Design and data processing of angle measurement system in construction machinery application," *Sensor world*, vol. 24, no. 8, pp. 7–13, Dec. 2018.
- [3] M. Ghanbari and M. Yazdanpanah, "Delay compensation of tilt sensors based on MEMS accelerometer using data fusion technique," *IEEE Sensors J.*, vol. 15, no. 3, pp. 1959–1966, Mar. 2015.
- [4] Z. Tong, Z. P. Wu, and W. Y. Lei, "High precision line-of-sight angle measurement method for dynamic aircraft based on phased array antenna," *Space Electron.*, vol. 14, no. 6, pp. 79–84, Dec. 2017.
- [5] K. Rao *et al.*, "A high-resolution area-change-based capacitive MEMS tilt sensor," *Sensors Actuators A: Phys.*, vol. 313, Mar. 2020, Art. no. 112191.
- [6] H. T. Tran Thi, N. D. Hai, A. N. Ngoc, D. N. Ngoc, L. V. Thai, and B. T. Tung, "A 3D printed two-axis tilt angle capacitive sensor," in *Proc. IEEE 7th Int. Conf. Commun. Electron.*, Hue city, Vietnam, 2018, pp. 191–195.
- [7] Y. C. Fu, W. Fan, H. X. Jin, and Q. Chen, "A new capacitance angle sensor of concentric ring multi-layer differential," *Measurement*, vol. 158, Feb. 2020, Art. no. 107625.
- [8] T. Schuthe, K. Junemann, and K. Riemschneider, "Tolerance compensation based on Gaussian processes for angle measurements with magnetic sensor arrays," in *Proc. IEEE Sensors*, Rotterdam, Netherlands, 2020, pp. 1–4.
- [9] S. Q. Su, D. C. Li, N. L. Tan, and G. Z. Li, "The study of a novel tilt sensor using magnetic fluid and its detection mechanism," *IEEE Sensors J.*, vol. 17, no. 15, pp. 4708–4715, Aug. 2017.
- [10] S. X. Wang, Z. Y. Wu, D. L. Peng, W. S. Li, S. Chen, and S. Y. Liu, "An angle displacement sensor using a simple gear," *Sensors Actuators A: Phys.*, vol. 270, pp. 245–251, Feb. 2018.
- [11] Y. G. Huang, S. Y. Zhang, L. Gao, and Y. L. Zheng, "Angle measurement technology based on magnetization vector for narrow space applications," *Nanotechnol. Precis. Eng.*, vol. 3, no. 3, pp. 167–173, Sep. 2020.
- [12] M. Jang, O. Kim, S. Yang, and J. Kim, "High bending curvature withstanding one dimensional angle sensor with fiber bragg gratings," in *Proc. IEEE Opt. Fiber Sensors Conf.*, Jeju, South Korea, 2017, pp. 1032397.
- [13] K. Ni, X. Y. Dong, Y. X. Jin, and H. S. Xu, "Temperature-independent fiber Bragg grating tilt sensor," *Microw. Opt. Technol. Lett.*, vol. 52, no. 10, pp. 2250–2252, Oct. 2010.
- [14] C. Li *et al.*, "Analyzing the applicability of side-polished fiber Bragg grating tilt sensor using liquid pendulum with controllable angle," in *Proc. IEEE Sensors*, Glasgow, U.K., 2017, pp. 1–3.
- [15] Y. Yang, X. B. Ma, K. Chen, E. Y. Wang, Z. H. Yu, and Q. X. Yu, "A high-resolution dynamic fiber-optic inclinometer," *Sensors Actuators A: Phys.*, vol. 283, pp. 305–312, Nov. 2018.
- [16] J. J. Pan, Q. M. Nan, S. J. Li, and Z. H. Hao, "Development of a high resolution optical-fiber tilt sensor by F-P filter," in *Proc IEEE Opt. Fiber Sensors Conf.*, Jeju, South, Korea, 2017, pp. 1–4.
- [17] C. Li, X. Li, X. Y. Yu, X. B. Peng, T. Lan, and S. C. Fan, "Room-Temperature wide measurement-range optical fiber Fabry-Perot tilt sensor with liquid marble," *IEEE Sensors J.*, vol. 18, no. 1, pp. 170–177, Jan. 2018.
- [18] B. O. Guan, H. Y. Tam, and S. Y. Liu, "Temperature-independent fiber Bragg grating tilt sensor," *IEEE Photon. Technol. Lett.*, vol. 16, no. 1, pp. 224–226, Jan. 2004.
- [19] O. Frazão, R. Falate, J. Fabris, J. Santos, L. Ferreira, and F. Araújo, "Optical inclinometer based on a single long-period fiber grating combined with a fused taper," *Opt. Lett.*, vol. 31, no. 20, pp. 2960–2962, 2006.
- [20] L. J. Arnaldo, F. Anselmo, M. Carlos, and J. P. Maria, "Polymer-optical-fiber-based sensor system for simultaneous measurement of angle and temperature," *Appl. Opt.*, vol. 57, no. 7, pp. 1717–1723, Mar. 2018.
- [21] P. G. Diego, S. Demetrio, and S. Salvador, "Analog radio over fiber links for future 5G radio access networks," in *Proc. 21st Int. Conf. Transparent Opt. Netw.* Angers, France, 2019, pp. 1–4.
- [22] L. D. Yanelis *et al.*, "Tip fiber-optic intermodal interferometer for refractive index sensing," *IEEE Photon. Technol. Lett.*, vol. 30, no. 1, pp. 15–18, Jan. 2018.
- [23] S. H. Liu, N. L. Liu, M. X. Hou, J. T. Guo, Z. H. Li, and P. X. Lu, "Direction-independent fiber inclinometer based on simplified hollow core photonic crystal fiber," *Opt. Lett.*, vol. 38, no. 4, pp. 449–451, 2013.
- [24] P. Yao, "Design and research of a conical optical fiber angle sensor," *Application Photoelectric Technol.*, vol. 32, no. 6, pp. 35–38, Jan. 2017.
- [25] X. T. Zhang, K. Ni, C. L. Zhao, M. P. Ye, and Y. X. Jin, "Tilt sensor based on intermodal photonic crystal fiber interferometer," *Photonic Sensors*, vol. 4, no. 3, pp. 209–214, Jul. 2014.
- [26] J. J. Wang, S. J. Tan, W. Zhang, Y. P. Li, Q. Sun, and D. M. Liu, "Inclinometer based on optical microfiber probes," in *Proc. Conf. Lasers Electro-Opt.*, CA, USA, 2019, pp. 1–2.
- [27] P. Hu, J. Guo, and J. Tan, "An annular planar-capacitive tilt sensor with a 360° measurement range," *IEEE Trans. Ind. Electron.*, vol. 63, no. 4, pp. 2469–2476, Apr. 2016.
- [28] D. Osman, X. L. Du, W. L. Li, and Y. Noh, "An optical joint angle measurement sensor based on an optoelectronic sensor for robot manipulators," in *Proc. 8th Int. Conf. Control, Mechatronics Automat.*, Moscow, Russia, 2020, pp. 28–32.
- [29] Y. X. Guo, C. Li, X. L. Zhou, L. Jiang, and H. H. Liu, "Wide-range fiber Bragg grating tilt sensor based on a cam structure," *Sensors J.*, vol. 20, no. 9, pp. 4740–4748, May 2020.
- [30] G. A. Miller, C. G. Askins, and G. A. Cranch, "Interferometric interrogation of a multicore fiber, two-axis inclinometer," in *Proc. SPIE - Int. Soc. for Opt. Eng.*, Edinburgh, U.K., 2009, Art. no. 75032R.
- [31] J. X. Cui, D. Gunawardena, Z. Y. Liu, Z. Zhao, and H. Y. Tam, "All-Fiber two-dimensional inclinometer based on Bragg gratings inscribed in a seven-core multi-core fiber," *J. Lightw. Technol.*, vol. 38, no. 8, pp. 2516–2522, Apr. 2020.
- [32] Y. T. Zhao, "Design and research of low frequency fiber grating space acceleration sensor," Master's thesis, Yanshan Univ., 2004, pp. 21–44.
- [33] S. Y. Peng, "Study on fiber Bragg grating axial traction sensing model," *J. Hunan Inst. Sci. Technol. (Natural Sci.)*, vol. 20, no. 2, pp. 35–37, Feb. 2007.
- [34] A. G. Leal-Junior, A. Theodosiou, M. Jimenez, R. Min, M. J. Pontes, and K. Kalli, "Plane-by-plane written, low-loss polymer optical fiber Bragg grating arrays for multiparameter sensing in a smart walker," *IEEE Sensors J.*, vol. 19, no. 20, pp. 9221–9228, Oct. 2019.
- [35] T. Paixão *et al.*, "Bragg gratings and Fabry-Perot interferometers on an Er-doped optical fiber," *Opt. Laser Technol.*, vol. 123, pp. 1–6, Nov. 2019.